

Article

Preparation of Orthorhombic WO₃ Thin Films and Their Crystal Quality-Dependent Dye Photodegradation Ability

Yuan-Chang Liang ^{1,*} and Che-Wei Chang ²

¹ Institute of Materials Engineering, National Taiwan Ocean University, Keelung 20224, Taiwan

² Undergraduate Program in Optoelectronics and Materials Technology, National Taiwan Ocean University, Keelung 20224, Taiwan; jf860218@gmail.com

* Correspondence: yuanvictory@gmail.com

Received: 8 January 2019; Accepted: 1 February 2019; Published: 2 February 2019



Abstract: Direct current (DC) magnetron sputtering deposited WO₃ films with different crystalline qualities were synthesized by postannealing at various temperatures. The in-situ DC sputtering deposited WO₃ thin film at 375 °C exhibited an amorphous structure. The as-grown WO₃ films were crystallized after annealing at temperatures of 400–600 °C in ambient air. Structural analyses revealed that the crystalline WO₃ films have an orthorhombic structure. Moreover, the crystallite size of the WO₃ film exhibited an explosive coarsening behavior at an annealing temperature above 600 °C. The density of oxygen vacancy of the WO₃ films was substantially lowered through a high temperature annealing procedure. The optical bandgap values of the WO₃ films are highly associated with the degree of crystalline quality. The annealing-induced variation of microstructures, crystallinity, and bandgap of the amorphous WO₃ thin films explained the various photoactivated properties of the films in this study.

Keywords: sputtering; annealing; crystal quality; photoactivated properties

1. Introduction

Tungsten oxide (WO₃), as a wide bandgap semiconductor, has been intensively investigated for various uses in scientific devices [1,2]. Among various applications, the photocatalyst application for degrading organic pollutants receives much attention as WO₃ has the advantages of low cost, high chemical stability, and excellent process-dependent reproducibility. In general, pure WO₃ crystal shows five phase transitions at temperatures ranging from –180 to 900 °C [3]. Among the five crystal forms, a monoclinic I WO₃ phase is the stable phase at room temperature. However, the orthorhombic WO₃ phase exists only in some WO₃ nanostructures at room temperature, not frequently visible for other morphologies such as a thin-film structure. This is attributable to the fact that the transition temperature of the orthorhombic WO₃ phase for WO₃ nanostructures is generally at room temperature, which is quite lower than that of bulk WO₃.

WO₃ in a thin-film structure is highly desirable for various device applications because thin solid film can be integrated into various small devices or combined with other materials to form composites for scientific applications. Several methods of manufacturing WO₃ thin films with various microstructures for applications have been reported. For example, the pulsed-laser deposited WO₃ thin films are integrated with TiO₂ thin films to form multilayer films and used for photodegradation of methylene blue (MB) solution. The WO₃ layer in the multilayer structure enhances the photocatalytic ability of the TiO₂ layer [4]. The spray pyrolysis synthesized WO₃ thin films have also been used for photodegrading methyl orange (MO) [5]. The thermal evaporation deposited WO₃ thin films with

adequate postannealing procedures in an oxygen-rich environment at 500 °C for 1 h have been used to degrade MB under irradiation [6]. Radio-frequency (RF) sputtering deposited WO₃/TiO₂ bilayer thin films with various WO₃ content are used to enhance the photocatalytic activity of TiO₂-based materials [7]. However, most WO₃ thin films synthesized through various methods are in a monoclinic structure; that is, the orthorhombic structure is limited in number.

Among various physical synthesis methods for WO₃ thin films, sputtering has been widely used to prepare oxide thin films with controllable microstructures and tunable physical properties. Moreover, the DC sputtering deposited WO₃ thin films via a metallic tungsten target provide the advantages of low cost and highly recycled usage of the target in comparison with those in WO₃ ceramic targeted by radio-frequency sputtering. Although DC sputtering growth of monoclinic or amorphous WO₃ thin films have been investigated for applications in gas-sensing, photocatalytic, and electrochromic devices, reports on the microstructure-dependent photodegradation properties of DC sputtering deposited orthorhombic WO₃ photocatalysts toward organic dyes are still lacking. Karuppasamy et al. synthesized amorphous WO₃ thin films via DC sputtering under various oxygen pressures. This work revealed that WO₃ films deposited at a lower working pressure exhibit satisfactory electrochromic properties. The variation of bulk density of the films prepared at various oxygen pressures affects the efficiency of insertion and removal of protons and electrons [8]. Kim et al. used DC sputtering to deposit monoclinic WO₃ films with various degrees of crystallinity by controlling the growth temperature from 200–500 °C. Higher crystal quality of WO₃ films deposited at a higher temperature resulted in better gas-sensing ability [9]. WO₃ films consisting of nanostructured surface feature are prepared by DC sputtering at various working pressures. The as-synthesized monoclinic WO₃ thin films are further used to photodegrade stearic acid [10]. Moreover, Stolze et al. prepared amorphous WO₃ films via DC sputtering under various O₂ percentages ranging from 0 to 20 vol.%; the effects of stoichiometry of WO₃ films on electrochromic properties were discussed [11]. The aforementioned examples demonstrate that most work on DC sputtering WO₃ films mainly focused on the monoclinic or amorphous phase. Reports on in-situ DC sputtering growth of orthorhombic WO₃ thin films are limited in number; this is associated with the fact that the orthorhombic structured WO₃ is unstable when the substrate temperature of the sputtering process is cooled down to room temperature. Therefore, the strategy to resolve this issue is to grow amorphous WO₃ films under a low oxygen content atmosphere, and then conduct various annealing procedures to obtain the stable orthorhombic WO₃ phase. Furthermore, the microstructure-dependent photocatalytic properties of the orthorhombic WO₃ films are presented in this study. The results herein might be useful for designing orthorhombic WO₃ thin-film photocatalysts with a desirable photodegradation ability toward organic dyes.

2. Methods

In this study, the WO₃ thin films were grown on 300 nm-thick SiO₂/Si and glass substrates by reactive DC magnetron sputtering at 375 °C. The metallic tungsten (purity > 99.99%) target was employed. The sputtering power of tungsten was kept at 40 W and the working pressure was maintained at 1.33 Pa during sputtering. The ratio of Ar/O₂ was fixed at 6:1. The thin film thickness was controlled to be 120 nm. The as-grown WO₃ films were subsequently annealed at 400–600 °C in ambient air for 1 h.

Scanning electron microscopy (SEM; S-4800, Hitachi, Tokyo, Japan) was used to investigate surface morphology of the WO₃ thin films. The surface roughness of various thin-film samples was measured by atomic force microscopy (AFM; D5000, Veeco Karlsruhe, Germany). Crystal structures of the films were investigated by X-ray diffraction (XRD; D2 Phaser, Bruker, Karlsruhe, Germany). The detailed microstructures of the films were studied by high-resolution transmission electron microscopy (HRTEM; JEM-2100F, JEOL Tokyo, Japan). An X-ray photoelectron spectroscope (XPS; PHI 5000 VersaProbe, ULVAC-PHI, Chigasaki, Japan) was used to understand the chemical binding states of the thin films' elements. The transmittance spectra of the thin films were measured using a UV-Vis spectrophotometer (V750, Jasco, Tokyo, Japan). Comparison of photocatalytic activity of various thin

films samples was performed using 10 mL methylene blue (MB; 10^{-6} M) solution containing various WO_3 thin films under various irradiation conditions. The change of MB solution concentration after photodegradation tests was analyzed by measuring the intensity variation of absorbance spectra using an UV-Vis spectrophotometer.

3. Result and Discussions

The change in crystal structure features of the WO_3 thin films with various thermal annealing procedures is depicted in Figure 1. The as-grown WO_3 film shows an amorphous structure, as no visible Bragg reflections are found. Figure 1 shows the XRD patterns of the WO_3 films with thermal annealing procedures at 400–600 °C. The orthorhombic crystalline WO_3 phase is formed with distinguishable Bragg reflections (JCDPS. 20-1324). The more intense Bragg reflections associated with a narrower full-width at half maximum were observed for the thin films annealed at a higher annealing temperature, revealing a higher degree of crystalline quality of the film. Notably, no other peaks of impurities were observed after thermal annealing procedures. The XRD results reveal that the as-grown WO_3 thin films exhibited a polycrystalline feature after postannealing. The crystallite sizes of the annealed WO_3 films were evaluated using the Scherrer formula [12]. The crystallite sizes of the WO_3 films annealed at 400, 500, and 600 °C were approximately 24, 32, and 57 nm, respectively. The (001)-oriented crystal dominated the crystal structure feature of the crystalline WO_3 thin films annealed below 500 °C; moreover, the (111)-oriented crystal dominated the crystal structure feature when the film was annealed at 600 °C. Notably, the change of the WO_3 crystal orientation from (001) to (111) at the higher temperature annealing is associated with the surface binding energy among the low index crystallographic planes [13].

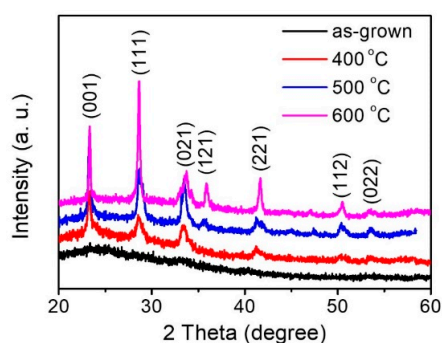


Figure 1. XRD patterns of the WO_3 films with and without thermal annealing procedures.

Surface morphologies of the WO_3 thin films with and without thermal annealing are shown in Figure 2. No distinctly well surface grain features can be seen for the as-grown WO_3 (Figure 2a). This might be associated with the amorphous nature of the sample as characterized by the XRD measurement. When the film was annealed at 400 °C, a surface grain feature was visible and the surface grains had an average size of approximately 32 nm (Figure 2b). Further increasing the annealing temperature to 500 °C increased the size of surface grains, and the homogeneity of grain size improved simultaneously. The average surface grain size was approximately 51 nm evaluated from Figure 2c. Notably, the surface grain size was abnormally increased (average grain size of 102 nm) and a uniformly cylindrical crystal feature was obtained when the film was annealed at 600 °C (Figure 2d). The high annealing temperature provides sufficient energy, which might facilitate the coalescence of the adjacent tiny crystals, and therefore large surface grains were formed.

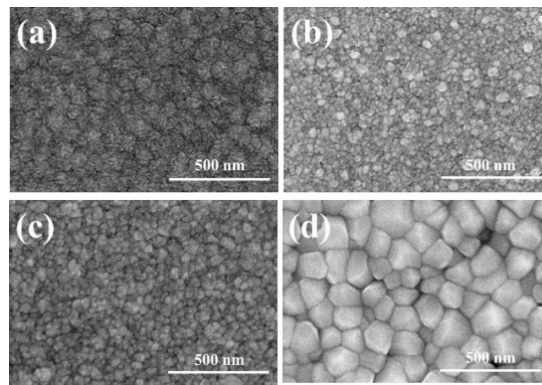


Figure 2. SEM images of the WO₃ thin films with and without annealing: (a) as-grown, (b) 400 °C, (c) 500 °C, (d) 600 °C.

Furthermore, the surface roughness of the various WO₃ thin films was further characterized by AFM. Figure 3a exhibits the surface of the as-grown WO₃ thin film. The root mean square (RMS) roughness of the as-grown amorphous WO₃ thin film was evaluated to be approximately 3.55 nm. Comparatively, the WO₃ thin films annealed at 400–600 °C exhibited coarser surface morphology (Figure 3b–d). The RMS roughness values of the WO₃ thin films were of approximately 4.02, 4.75, and 9.28 nm corresponding to the annealing temperature of 400, 500, and 600 °C, respectively. This result demonstrated that the surface roughness monotonically increases with increasing annealing temperature because high annealing temperature facilitates the coalescence of the surface grains and therefore rougher surface. The average surface grain sizes of the WO₃ thin films annealed at 400, 500, and 600 °C were approximately 26, 43, and 84 nm, respectively. Larger surface grains of the annealed film engendered a rougher surface feature. Similarly, a substantially increased surface grain size, as reported in the CuO film, annealed at the temperature higher than 700 °C [14].

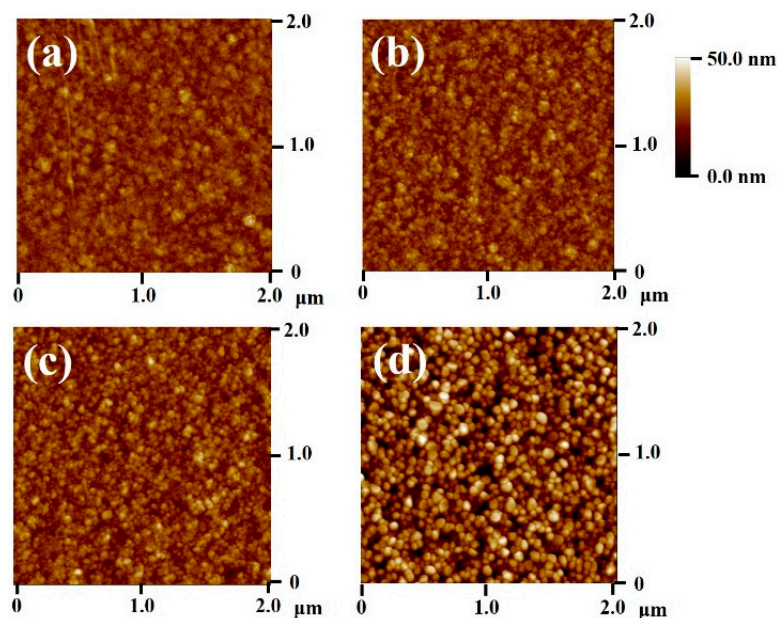


Figure 3. AFM images of WO₃ thin films with and without annealing: (a) as-grown, (b) 400 °C, (c) 500 °C, (d) 600 °C.

The detailed microstructures of the WO_3 thin films with and without thermal annealing at $600\text{ }^\circ\text{C}$ were investigated by TEM. A low-magnification, cross-sectional TEM image of the as-grown WO_3 thin film is shown in Figure 4a. The thickness of the WO_3 film was $\sim 120\text{ nm}$. The film surface is dense and smooth, and no voids can be seen. A high-resolution TEM (HRTEM) micrograph of the as-grown WO_3 thin film is depicted in Figure 4b. The random and chaotic lattice fringes with a short-range order are distributed over the area of interest, revealing that the film is in the amorphous phase. Moreover, the selected area electron diffraction (SAED) pattern in Figure 4c exhibits a faint ring-like pattern, revealing that the film without heat treatment is uncrystallized. This is in agreement with the XRD result. Figure 4d depicts the energy-dispersive X-ray spectroscopy (EDS) spectra of the film, confirming that the film's composition consisted of W and O. Moreover, the O/W composition ratio is approximately 2.48, demonstrating oxygen deficiency in the WO_3 thin film. This is often observed in oxide thin films prepared by sputtering because the thin film growth condition is in an oxygen deficient environment during sputtering [15].

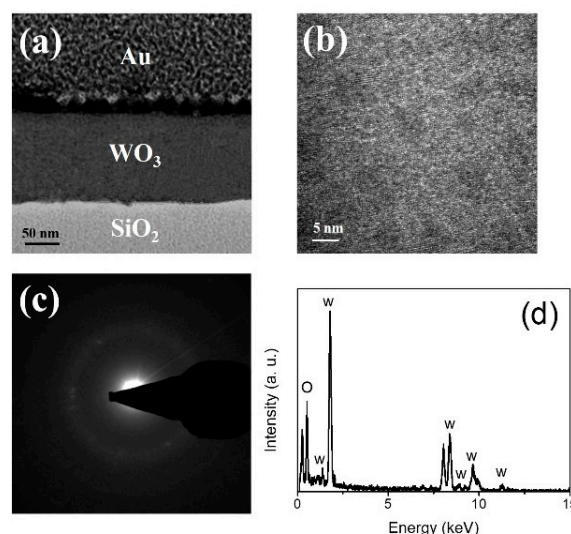


Figure 4. TEM analysis of the as-grown WO_3 film: (a) low-magnification image, (b) high-resolution image, (c) SAED pattern, (d) EDS spectra.

Figure 5a depicts a low-magnification, cross-sectional image of the WO_3 film annealed at $600\text{ }^\circ\text{C}$. The film thickness of the annealed WO_3 film is homogeneous throughout its cross section. Compared to the as-grown film, the surface and root of the high-temperature-annealed film are more undulated. Figure 5b,c demonstrate HRTEM images of the annealed WO_3 thin film. The appearance of visible and ordered lattice fringes in the HREM images indicate that the WO_3 film after annealing had a high degree of crystallinity. The atomic lattice fringes with intervals of approximately 0.39, 0.31, and 0.27 nm could be identified and were attributed to the interplanar distances of the WO_3 (001), (111), and (021) crystallographic planes, respectively. The boundaries between the adjacent grains were visible. The polycrystalline nature and the orthorhombic structure of the WO_3 film were also confirmed by the SAED measurements in Figure 5d. Distinct diffraction spots arranged in centric rings revealed the crystalline WO_3 thin film was formed after the $600\text{ }^\circ\text{C}$ annealing process. Figure 5e shows the EDS spectra; the spectra revealed that the film mainly composed of W and O. No other impurity atoms were detected.

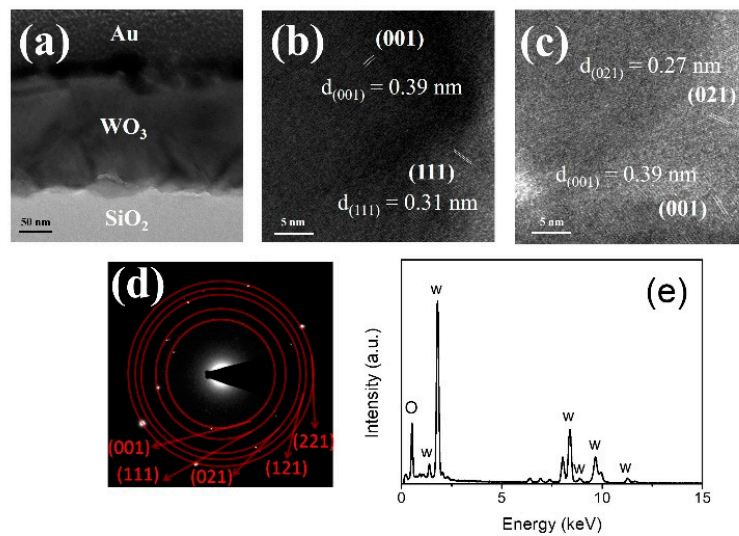


Figure 5. TEM analysis of the WO_3 film annealed at $600\text{ }^\circ\text{C}$: (a) low-magnification image, (b,c) HR images, (d) SAED pattern, (e) EDS spectra.

XPS analysis was performed to reveal the elemental binding states of various WO_3 thin films. The annealing temperature-dependent W oxidation state change is shown in Figure 6a–d. From the figures, the intense doublet with binding energies of approximately 35.0 eV ($\text{W}4f_{7/2}$) and 37.2 eV ($\text{W}4f_{5/2}$) are associated with photoelectrons emitted from W^{6+} ions of the WO_3 films, while the relatively small peaks at 34.0 and 36.2 eV can be assigned to $\text{W}4f_{7/2}$ and $\text{W}4f_{5/2}$ of W^{5+} oxidation state in tungsten oxides [16]. The presence of W^{5+} suggests the existence of crystal defects in the WO_3 film. Comparatively, the area and the height of core level W^{5+} decreased after annealing, which implied increased oxidation states of W in the WO_3 film. Notably, the WO_3 film annealed at $600\text{ }^\circ\text{C}$ had the smallest features of W^{5+} , which indicates the surface tungsten in this film exhibited a larger degree of oxidation state after annealing. No peaks attributed to metallic W were identified in the spectra of all films. Notably, the W/O atomic ratio of the as-grown WO_3 film was approximately 0.4. Moreover, the W/O atomic ratio of the WO_3 films decreased from 0.37 to 0.34 with the annealing temperature increasing from 400 to $600\text{ }^\circ\text{C}$, respectively, evaluated from the XPS analyses. Figure 6e–h show that the XPS spectra of O1s for various WO_3 thin films have an asymmetric curve feature. The O1s spectra of the surface of various WO_3 thin films were fitted by two distributions, centered at approximately 529.3 and 530.8 eV, respectively. The relatively low binding energy peak is attributed to O^{2-} ions in the oxide lattice. The higher binding energy peak is attributed to the oxygen vacancies in the WO_3 [17]. The relative content of the oxygen vacancy for various WO_3 films was evaluated according to the area ratio of these two deconvolution components: (red peak)/(red peak + blue peak). The relative area of the higher energy binding component for the WO_3 films decreased with the annealing temperature. A great amount of vacancy existed in the surface of the as-grown WO_3 film. After annealing, the surface oxygen vacancy content markedly decreased from 34.4% to 25.3% with the annealing temperature increasing from 400 to $600\text{ }^\circ\text{C}$, respectively.

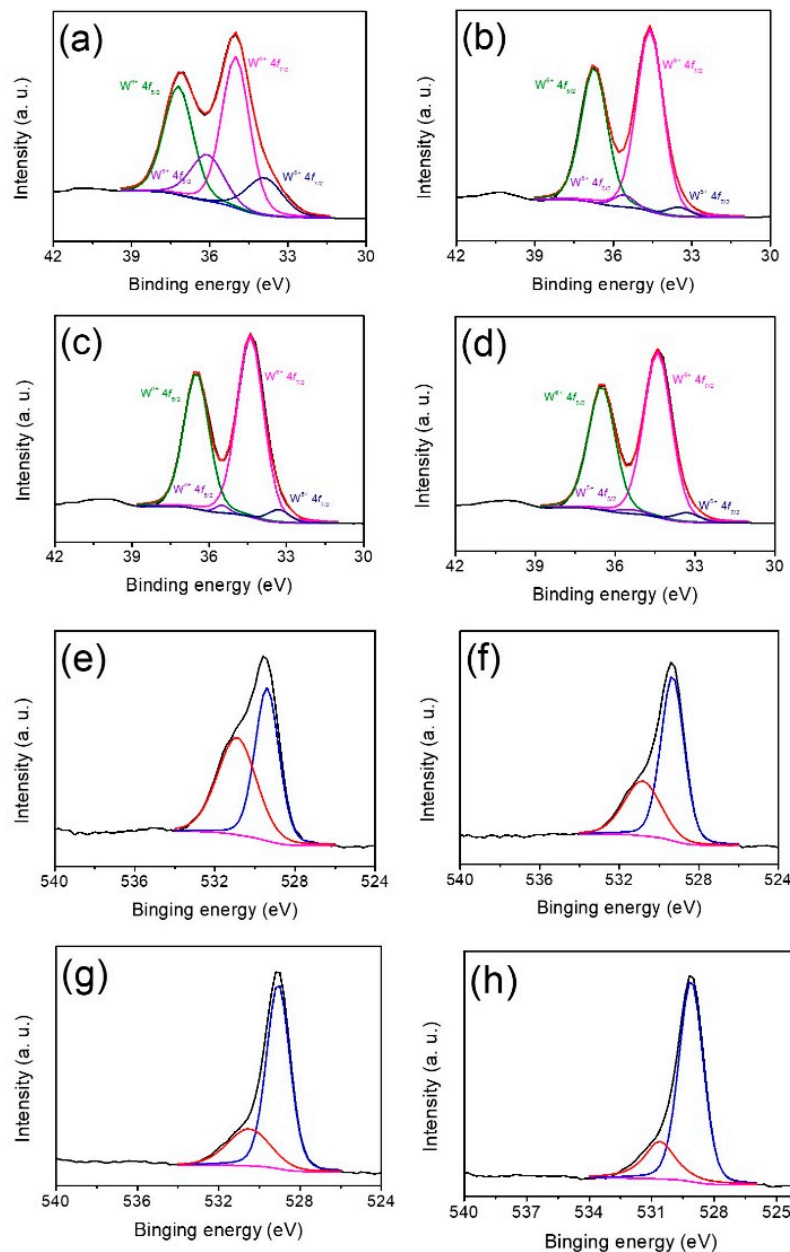


Figure 6. W4f XPS narrow scan spectra of the WO_3 thin films with and without annealing: (a) as-grown, (b) 400 °C, (c) 500 °C, (d) 600 °C. O1s XPS narrow scan spectra of the WO_3 thin films with and without annealing: (e) as-grown, (f) 400 °C, (g) 500 °C, (h) 600 °C.

The transmittance spectra of the WO_3 thin films with and without annealing are demonstrated in Figure 7a. The light was highly absorbed in the visible region with less than 40% transmittance for the as-grown WO_3 film, attributed to the presence of massive oxygen-related defects. Moreover, the as-grown WO_3 film is seen in semi-transparent bluish color, which shows the amorphous and highly non-stoichiometric natures of the film [18]. The highly transparent feature was observed for the WO_3 films conducted with annealing; moreover, no blue colouration appeared in the samples. The enhancement in the transmittance degree of the annealed WO_3 films is due to the reduction of oxygen-related crystal defects, which might play an important role in scattering the incident light. Notably, a clear shoulder feature appeared at approximately 350 nm for the films annealed below 600 °C. That shoulder feature in the optical transmittance spectra is associated with the residual crystal defects associated with oxygen deficiencies in the samples [19]. Notably, the shoulder feature

completely vanished for the WO_3 film conducted with thermal annealing at $600\text{ }^\circ\text{C}$, indicating that the oxygen-related crystal defects of the film were substantially removed in the annealing process. The bandgap value of various thin-film samples is calculated by plotting $(\alpha h\nu)^{1/2}$ vs. photon energy using the following formula:

$$\alpha h\nu = A(h\nu - E_g)^n \quad (1)$$

where α is the absorption coefficient, A is a constant, $h\nu$ is the energy of an incident photon, E_g is the bandgap value. On extrapolating the linear portion of the curves (Figure 7b), the intercept on the energy axis ($(\alpha h\nu)^{1/2} = 0$) gives the value of the indirect bandgap energy. The bandgap values were calculated as 2.48, 3.04, 3.04, and 2.78 eV for as-grown and annealed WO_3 samples at 400, 500, and $600\text{ }^\circ\text{C}$, respectively. The as-prepared WO_3 thin film exhibited the smallest bandgap value and may be associated with a relatively large content of oxygen deficiencies in the film as compared to the annealed ones. Due to the existence of a high density of oxygen-deficient crystal defects, they might form new discrete energy bands below the conduction band, resulting in the relatively low band gap. After annealing at 400 and $500\text{ }^\circ\text{C}$, the E_g of two WO_3 thin-film samples originates from the recombination of free carriers from the bottom of the conduction band energy to the valence band energy with the decreased discrete energy bands after thermal annealing. It was noticed that the bandgap value of the WO_3 film further decreased at the highest annealing temperature of $600\text{ }^\circ\text{C}$, assigned to explosive growth in grain size of the WO_3 film [20].

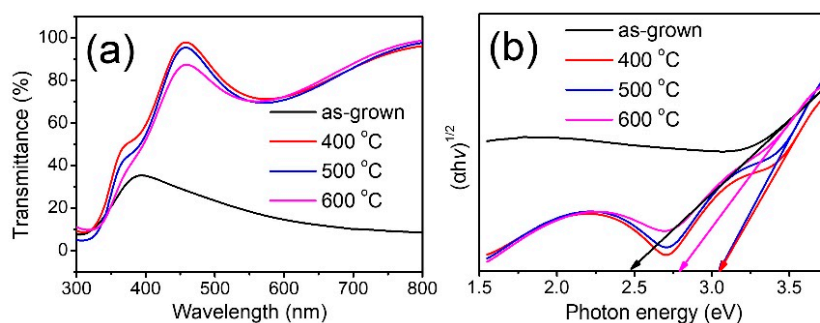


Figure 7. (a) Optical transmittance spectra of various WO_3 films, (b) Tauc plot of various WO_3 films.

Figure 8a–d show the absorbance spectra of the MB solution in the presence of various WO_3 thin films at different irradiation times. After the MB solution was illuminated, the absorbance peak intensity at $\sim 663\text{ nm}$ was observed to gradually decrease with duration, implying that MB molecules are photodegraded. The photodegradation degrees (C/C_0) of the MB solution containing various WO_3 thin films are summarized in Figure 7e. The C_0 is concentration MB solution without irradiation and C is the residual concentration of the MB solution after irradiation at a given duration. Notably, the C/C_0 values of the MB solution containing various WO_3 thin films under various dark conditions are demonstrated in Figure 7e. A slightly decrease of C/C_0 value was observed for the dark balance of 120 min; this is attributed to the fact that partial MB molecules were absorbed on the surface of the WO_3 thin films under dark balance condition. By contrast, the photodegradation rates of the MB solution with various WO_3 thin films are different. As demonstrated in Figure 8e, the WO_3 film conducted with thermal annealing at $600\text{ }^\circ\text{C}$ was most catalytically efficient, giving a photodegradation extent of approximately 45% in 30 min, while other annealed thin films photodegraded only 35% of MB in the same time period. After 120 min irradiation, the WO_3 film annealed at $600\text{ }^\circ\text{C}$ still displayed the largest degree of photodegradation toward the MB solution. Notably, under irradiation, WO_3 was photoexcited and the e^-/h^+ pairs were formed. The e^- can participate in organic pollutant degradation reactions. The possible formations of the superoxide anion, hydroperoxyl, and hydrogen peroxide (H_2O_2) species in the organic dye solution are advantageous for further degrading the MB dyes [21]. However, it has been shown that the position of the conduction band of WO_3 (+0.50 V vs. NHE) was below the standard redox potential for the formation of superoxide anion (-0.33 V

vs. NHE) and hydroperoxyl (-0.046 V vs. NHE) [22]. Based on the aforementioned, the following reactions are therefore more likely to occur during the MB photodegradation process using WO_3 thin films as photocatalysts:

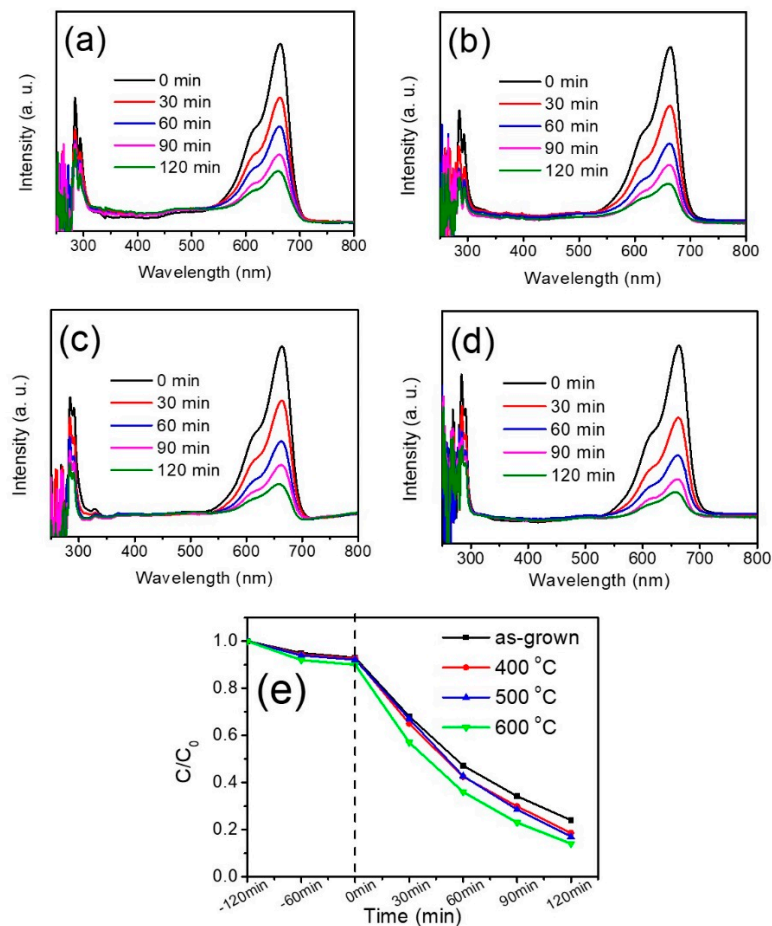
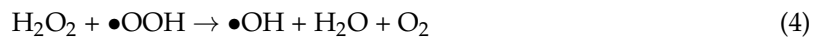


Figure 8. The intensity variation of absorbance spectra of the MB solution in presence of various WO_3 thin films under different irradiation durations: (a) as-grown, (b) 400 °C, (c) 500 °C, (d) 600 °C, (e) Plot of C/C_0 vs. irradiation time.

Meanwhile, the photogenerated h^+ in the WO_3 might involve the reactions and form $\bullet\text{OH}$ radicals through the following equations:



The produced $\bullet\text{OH}$ radicals are efficiently degrading species for the MB dyes. Although the band position of the WO_3 is advantageous for the photodegradation mechanism, the microstructure and optical properties should be considered for the final photodegradation efficiency. The WO_3 film with thermal annealing performed at 600 °C was the most active photocatalyst, and the films annealed at lower temperatures were somewhat less active in this work. In contrast, the as-grown WO_3 film had a lower photocatalytic activity. We assume that the deteriorated crystal quality of the WO_3 with the lower annealing temperatures or without annealing was the decisive factor in their inferior photodegradation

activity. Fewer oxygen-deficient-related defects in the lattice of the WO₃ film annealed at 600 °C might result in fewer recombination centers in the film, which would be detrimental for the higher photodegradation efficiency in this study. Moreover, the relative lower optical bandgap value of the WO₃ film conducted with thermal annealing at 600 °C among different annealed thin films is another advantageous factor to increase the light harvesting and enhance the degradation ability of crystalline WO₃ film toward MB dyes under irradiation.

4. Conclusions

The WO₃ thin films were DC sputtering deposited at 375 °C; moreover, the as-grown films exhibited an amorphous structure because of large composition deviation from the stoichiometric value. The as-grown WO₃ thin films were further conducted by thermal annealing procedures at 400–600 °C in ambient air. Structural analyses revealed that the amorphous WO₃ thin films crystallized after thermal annealing and demonstrated an orthorhombic structure. The surface grain size and surface roughness of the WO₃ films increased with annealing temperature. Moreover, the density of oxygen-deficiency-related crystal defects in the WO₃ films decreased with annealing temperature. The optical bandgap of WO₃ thin films are highly associated with the crystal quality and this can be controlled by conducting with different thermal annealing procedures. The as-grown WO₃ thin film annealed at 600 °C exhibited the highest photodegradation ability toward organic dyes in this study because of its high crystallinity, low crystal defects, and low optical bandgap among the various WO₃ thin films herein.

Author Contributions: Formal Analysis, C.-W.C.; Investigation, Y.-C.L. and C.-W.C.; Writing—Original Draft Preparation, Y.-C.L. and C.-W.C.; Writing—Review and Editing, Y.-C.L.; Supervision, Y.-C.L.

Funding: This research was funded by the Ministry of Science and Technology of Taiwan (MOST 105-2628-E-019-001-MY3).

Conflicts of Interest: The authors declare no conflict of interest.

References

1. Dong, P.; Hou, G.; Xi, X.; Shao, R.; Dong, F. WO₃-based photocatalysts: Morphology control, activity enhancement and multifunctional applications. *Environ. Sci. Nano* **2017**, *4*, 539–557. [[CrossRef](#)]
2. Lee, W.H.; Lai, C.W.; Hamid, S.B.A. One-step formation of WO₃-loaded TiO₂ nanotubes composite film for high photocatalytic performance. *Materials* **2015**, *8*, 2139–2153. [[CrossRef](#)]
3. Faudoa-Arzate, A.; Arteaga-Durán, A.; Saenz-Hernández, R.J.; Botello-Zubiate, M.E.; Realyvazquez-Guevara, P.R.; Matutes-Aquino, J.A. HRTEM microstructural characterization of β-WO₃ thin films deposited by reactive RF magnetron sputtering. *Materials* **2017**, *10*, 200. [[CrossRef](#)] [[PubMed](#)]
4. Shinguu, H.; Bhuiyan, M.M.H.; Ikegami, T.; Ebihara, K. Preparation of TiO₂/WO₃ multilayer thin film by PLD method and its catalytic response to visible light. *Thin Solid Films* **2006**, *506*, 111–114. [[CrossRef](#)]
5. Hunge, Y.M.; Mahadik, M.A.; Kumbhar, S.S.; Mohite, V.S.; Rajpure, K.Y.; Deshpande, N.G.; Moholkar, A.V.; Bhosale, C.H. Visible light catalysis of methyl orange using nanostructured WO₃ thin films. *Ceram. Int.* **2016**, *42*, 789–798. [[CrossRef](#)]
6. Arfaoui, A.; Touihri, S.; Mhamdi, A.; Labidi, A.; Manoubi, T. Structural, morphological, gas sensing and photocatalytic characterization of MoO₃ and WO₃ thin films prepared by the thermal vacuum evaporation technique. *Appl. Surf. Sci.* **2015**, *357*, 1089–1096. [[CrossRef](#)]
7. Dobromir, M.; Apetrei, R.P.; Rebegea, S.; Manole, A.V.; Nica, V.; Luca, D. Synthesis and characterization of RF sputtered WO₃/TiO₂ bilayers. *Surf. Coat. Technol.* **2016**, *285*, 197–202. [[CrossRef](#)]
8. Subrahmanyam, A.; Karuppasamy, A. Electrochromism. Optical and electrochromic properties of oxygen sputtered tungsten oxide (WO₃) thin films. *Sol. Energy Mater. Sol. Cells* **2007**, *91*, 266–274. [[CrossRef](#)]
9. Kim, T.S.; Kim, Y.B.; Yoo, K.S.; Sung, G.S.; Jung, H.J. Sensing characteristics of dc reactive sputtered WO₃ thin films as an NO_x gas sensor. *Sens. Actuators B Chem.* **2000**, *62*, 102–108. [[CrossRef](#)]

10. Johansson, M.; Niklasson, G.; Österlund, L. Structural and optical properties of visible active photocatalytic WO₃ thin films prepared by reactive dc magnetron sputtering. *J. Mater. Res.* **2012**, *27*, 3130–3140. [[CrossRef](#)]
11. Stolze, M.; Gogova, D.; Thomas, L.-K. Analogy for the maximum obtainable colouration between electrochromic, gasochromic, and electrocolouration in DC-sputtered thin WO_{3-y} films. *Thin Solid Films* **2005**, *476*, 185–189. [[CrossRef](#)]
12. Warren, B.E. *X-ray Diffraction*; Addison Wesley Publishing Co.: London, UK, 1969.
13. Liu, H.; Lu, H.; Zhang, L.; Wang, Z. Orientation selection in MgO thin films prepared by ion-beam-deposition without oxygen gas present. *Nucl. Instrum. Methods Phys. Res. B* **2015**, *360*, 60–63. [[CrossRef](#)]
14. Masudy-Panah, S.; Moakhar, R.S.; Chua, C.S.; Kushwaha, A.; Wong, T.I.; Dalapati, G.K. Rapid thermal annealing assisted stability and efficiency enhancement in a sputter deposited CuO photocathode. *RSC Adv.* **2016**, *6*, 29383–29390. [[CrossRef](#)]
15. Liang, Y.C.; Liang, Y.C. Physical properties of low temperature sputtering-deposited zirconium-doped indium oxide films at various oxygen partial pressures. *Appl. Phys. A* **2009**, *97*, 249–255. [[CrossRef](#)]
16. Hussain, T.; Al-Kuhaili, M.F.; Durrani, S.M.A.; Qurashi, A.; Qayyum, H.A. Enhancement in the solar light harvesting ability of tungsten oxide thin films by annealing in vacuum and hydrogen. *Int. J. Hydrog. Energy* **2017**, *42*, 28755–28765. [[CrossRef](#)]
17. Nayak, A.K.; Ghosh, R.; Santra, S.; Guha, P.K.; Pradhan, D. Hierarchical nanostructured WO₃-SnO₂ for selective sensing of volatile organic compounds. *Nanoscale* **2015**, *7*, 12460–12473. [[CrossRef](#)] [[PubMed](#)]
18. Castro-Hurtado, I.; Tavera, T.; Yurrita, P.; Pérez, N.; Rodriguez, A.; Mandayo, G.G.; Castaño, E. Structural and optical properties of WO₃ sputtered thin films nanostructured by laser interference lithography. *Appl. Surf. Sci.* **2013**, *276*, 229–235. [[CrossRef](#)]
19. Bujji Babu, M.; Madhuri, K.V. Structural, morphological and optical properties of electron beam evaporated WO₃ thin films. *J. Taibah Univ. Sci.* **2017**, *11*, 1232–1237.
20. Jain, P.; Arun, P. Influence of grain size on the band-gap of annealed SnS thin films. *Thin Solid Films* **2013**, *548*, 241–246. [[CrossRef](#)]
21. Aslam, I.; Cao, C.; Khan, W.S.; Tanveer, M.; Abid, M.; Idrees, F.; Riasat, R.; Tahir, M.; Butt, F.K.; Ali, Z. Synthesis of three-dimensional WO₃ octahedra: Characterization, optical and efficient photocatalytic properties. *RSC Adv.* **2014**, *4*, 37914–37920. [[CrossRef](#)]
22. Ghosh, A.; Mitra, M.; Banerjee, D.; Mondal, A. Facile electrochemical deposition of Cu₇Te₄ thin films with visible-light driven photocatalytic activity and thermoelectric performance. *RSC Adv.* **2016**, *6*, 22803–22811. [[CrossRef](#)]

